Ternary Hybrids of Amorphous Nickel Hydroxide–Carbon Nanotube-Conducting Polymer for Supercapacitors with High Energy Density, Excellent Rate Capability, and Long Cycle Life

*Wenchao Jiang, Dingshan Yu, Qiang Zhang, Kunli Goh, Li Wei, Yili Yong, Rongrong Jiang, Jun Wei, and Yuan Chen**

The utilization of $Ni(OH)_2$ as a pseudocapacitive material for high performance supercapacitors is hindered by its low electrical conductivity and short cycle life. A coaxial ternary hybrid material comprising of amorphous $Ni(OH)_2$ deposited on multiwalled carbon nanotubes wrapped with conductive polymer (poly (3,4-ethylenedioxythiophene)-poly(styrenesulfonate)) is demonstrated. A thin layer of disordered amorphous $Ni(OH)_2$ is deposited by an effective "coordinating etching and precipitating" method, resulting in an ultrahigh specific capacitance of 3262 F g^{-1} at 5 mV s^{-1} and excellent rate capability (71.9% capacitance retention at 100 mV s^{-1}). More importantly, the polymer layer prevents the degradation of the nanostructure and dissolution of Ni ion during repeated charge–discharge cycling for 30 000 cycles, a phenomenon which often plagues $Ni(OH)_2$ nanomaterials. Using the ternary $Ni(OH)_2$ hybrid and the reduced graphene oxide/carbon nanotube hybrid as the positive and negative electrodes, respectively, the assembled asymmetric supercapacitors exhibit high energy density of 58.5 W h kg^{-1} at the power density of 780 W kg^{-1} as well as long cycle life (86% capacitance retention after 30 000 cycles). The ternary hybrid architecture design for amorphous $Ni(OH)_2$ can be regarded as a general approach to obtain pseudocapacitive materials for supercapacitors with both high energy density, excellent rate capability, and long cycle life.

1. Introduction

Supercapacitors or electrochemical capacitors have attracted significant interests because they can deliver 10–100 times higher energy per unit time (i.e., high power density) than most batteries, be safely charged/discharged at high current in less than a minute (i.e., high rate capability), and withstand tens of thousands of charge/discharge cycles without losing their original energy storage capacity (i.e., long cycle life).[1,2] However, supercapacitors store approximately 10% of energy per unit volume or mass (i.e., low energy density) compared to batteries. The energy storage of supercapacitors is based on two principles: electrical double-layer capacitance (EDLC) and pseudocapacitance. EDLC stores electrostatic energy by adsorption of electrolyte ions onto the surface of electrode materials.[1] As no ion diffusion in bulk electrode materials is required in EDLC, the response to potential changes is rapid, leading to a high power. However, the ion adsorption is restricted to the surface, so the energy density from EDLC is limited.[3] Pseudocapacitance originates from reversible redox reactions, intercalation or electrosorption at or near the surface of some electrode materials. Commonly used pseudocapacitive materials include transition metal oxides and hydroxides, such as RuO_2, MnO_2, $Ni(OH)_2$, $Co(OH)_2$, NiO, Co_3O_4, etc., nitrides, carbides, and conducting polymers, such as polyaniline, polypyrrole, polythiophene, etc.[4–6] The pseudocapacitance can be as large as ten times that of EDLC in some supercapacitors, leading to high energy density supercapacitors. However, the increase in energy density in such supercapacitors often comes at the price of lower power density, poorer rate capability, and shorter cycle life. This is because redox reactions in the bulk of pseudocapacitive materials are diffusion-controlled, resulting in sluggish reaction kinetics and low Coulombic efficiency.[3] To this end, engineering pseudocapacitive materials at the nanoscale level to allow a large fraction of redox reactions to

W. Jiang, Dr. D. Yu, K. Goh, Dr. L. Wei, Y. Yong, Prof. R. Jiang, Prof. Y. Chen
School of Chemical and Biomedical Engineering
Nanyang Technological University
62 Nanyang Drive 637459, Singapore
E-mail: chenyuan@ntu.edu.sg
Prof. Q. Zhang
Beijing Key Laboratory of Green Chemical Reaction Engineering and Technology
Department of Chemical Engineering
Tsinghua University
No. 1, Tsinghuayuan, Beijing 100084, P.R. China
Dr. J. Wei
Singapore Institute of Manufacturing Technology
71 Nanyang Drive 638075, Singapore

DOI: 10.1002/adfm.201403354

take place on the surface or near-surface region of pseudocapacitive materials is particularly paramount to the development of supercapacitors with both high energy density, high rate capability, and long cycle life.

$Ni(OH)_2$/NiO(OH) couple is the main redox system used in the positive electrodes of alkaline rechargeable batteries, because of its good reversibility and cyclic behavior.[5,6] $Ni(OH)_2$ has also attracted great interest as pseudocapacitive materials for supercapacitors due to its high theoretical specific pseudocapacitance of 2082 F g^{-1} (in a potential window of 0.5 V), environmental friendliness, and low cost.[7] In particular, $Ni(OH)_2$ in amorphous phase is expected to have better electrochemical efficiency due to more grain boundaries and ion diffusion channels in the disordered structure compared to the crystalline phase.[7,8] The key issues of applying $Ni(OH)_2$ in practical supercapacitors lie in its low electrical conductivity and short cycle life. The electrical conductivity of $Ni(OH)_2$ is very low at around 10^{-15} Ω^{-1} m^{-1}.[9] Thus, the redox reactions can only take place on its surface, and most of $Ni(OH)_2$ is inaccessible to electrolyte ions and remains as dead volume in supercapacitors.[10,11] Several approaches have been explored to address the issues caused by the low electrical conductivity of $Ni(OH)_2$, including synthesis of porous structures, nanoparticles, thin films, and nanosheets to expose more $Ni(OH)_2$ surfaces to electrolyte ions,[12,13] forming $Ni(OH)_2$ and carbon materials or conducting polymers hybrids to have imbedded conductive networks,[14–18] introducing other metal ions into $Ni(OH)_2$ to enhance its conductivity.[17,19,20] Even though these nanoscale engineering approaches can improve the electrical conductivity of $Ni(OH)_2$, the constructed nanoscale structures often degrade and Ni ions dissolve into electrolytes after repeated charge/discharge cycles, which can result in short cycle life of supercapacitors.[5,13,14,20–22]

In this study, with the aim of constructing supercapacitors with both high energy density, good rate capability, and long cycle life, we have designed and synthesized a novel ternary hybrid electrode material comprising of multiwalled carbon nanotubes (MWCNTs), amorphous(amor)-$Ni(OH)_2$ and poly (3,4-ethylenedioxythiophene)-poly(styrenesulfonate) (PEDOT:PSS) as high performance pseudocapacitive materials. Other than the commonly used crystalline $Ni(OH)_2$, a thin layer of disordered amor-$Ni(OH)_2$ was deposited on conductive acid-treated MWCNTs by using a "coordinating etching and precipitating" method, which enabled efficient redox reactions to take place mostly on the surface of $Ni(OH)_2$. To prevent the dissolution of Ni ions into electrolytes and preserve the nanoscale structures amor-$Ni(OH)_2$ upon long charge/discharge cycles, a conductive polymer layer was further wrapped around the MWCNT/amor-$Ni(OH)_2$. Such a unique hybrid architecture design results in $Ni(OH)_2$ pseudocapacitive materials with ultrahigh specific capacitance and long cycle life. Asymmetric supercapacitors fabricated with the MWCNT/amor-$Ni(OH)_2$/PEDOT:PSS as positive electrodes and reduced graphene oxide (rGO)/CNT hybrids as negative electrodes have demonstrated one of the highest energy densities among $Ni(OH)_2$-based supercapacitors with excellent rate capability and long cycle life.

2. Results and Discussion

2.1. Synthesis of Hybrid Materials

It has been a significant challenge to directly synthesize amor-$Ni(OH)_2$, because all commonly used methods result in crystalline $Ni(OH)_2$.[13] We have utilized a two-step procedure to achieve this as illustrated in **Figure 1**. First, Cu_2O nanocrystals were anchored onto the nitric acid-treated MWCNTs[23] through in situ reduction of $Cu(OH)_2$ to Cu_2O by ascorbic acid (Vitamin C, $C_6H_8O_6$) at room temperature. Next, the "coordinating etching and precipitating" method was used to replace Cu_2O nanocrystals with amor-$Ni(OH)_2$.[24] Alkaline $S_2O_3^{2-}$ ions etched Cu_2O to generate Cu^+ and OH^- ions. The OH^- ions synchronously combined with Ni^{2+} to form amor-$Ni(OH)_2$. The chemical reactions are as shown

$$Cu_2O + xS_2O_3^{2-} + H_2O \rightarrow [Cu_2(S_2O_2)_x]^{2-2x} + 2OH^- \quad (1)$$

$$Ni^{2+} + 2OH^- \rightarrow Ni(OH)_2 \quad (2)$$

Amor-$Ni(OH)_2$ was deposited on the MWCNTs, resulting in a coaxial hybrid denoted as MWCNT/amor-$Ni(OH)_2$. The coaxial hybrid was further wrapped with the water soluble conducting polymer at a mass ratio of 9:1 between MWCNT/amor-$Ni(OH)_2$ and PEDOT:PSS to form the final MWCNT/amor-$Ni(OH)_2$/PEDOT:PSS ternary hybrid. In this ternary architecture design, we took advantage of the following synergistic effects. First, MWCNT with excellent conductivity, large specific surface area, and relatively low cost serves as an ideal conductive template for the amor-$Ni(OH)_2$ deposition. Second, instead of crystalline $Ni(OH)_2$, either α-crystalline or β-crystalline $Ni(OH)_2$, which is commonly used as pseudocapacitive material,[15,16,25–27] amor-$Ni(OH)_2$ is chosen in this work since disorders in crystalline $Ni(OH)_2$ can greatly improve their electrochemical efficiency.[8,11] However, few studies have employed amor-$Ni(OH)_2$ in supercapacitors because of its synthesis difficulty. Recently, a few methods including freezing microemulsion[28] and high voltage electrolysis[13] were reported to produce bulk amor-$Ni(OH)_2$. In this study, we have applied a simple but effective "coordinating etching and precipitating" method to deposit a thin layer of amor-$Ni(OH)_2$ on the MWCNTs. Third, wrapping of the MWCNT/amor-$Ni(OH)_2$ with a conducting polymer can significantly reduce the contact resistance among the metal oxide/hydroxide deposited MWCNTs as observed in previous

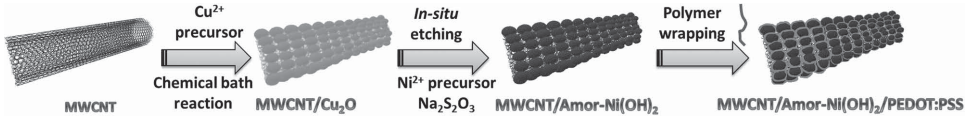

Figure 1. Schematic illustration of the MWCNT/amor-$Ni(OH)_2$/PEDOT:PSS ternary hybrid synthesis procedure.

studies,[10,29,30] while achieving a long cycle life by preventing the irreversible dissolution of Ni ions from the amor-$Ni(OH)_2$ into electrolytes. Such conducting polymers have the potentials to replace insulating polymer binders, such as polytetrafluoroethylene and polyvinylidene fluoride (PVDF), commonly used in supercapacitor electrode fabrication.[10]

2.2. Structural Characterization of the Hybrids

The morphologies of the synthesized hybrid materials were first examined by scanning electron microscope (SEM). The nitric acid-treated MWCNTs have a diameter of 10–15 nm with their structure intact after introducing carboxyl groups on their side walls (Figure S1a, Supporting Information). After depositing Cu_2O, their diameters increase to around 20 nm (Figure S1b, Supporting Information). **Figure 2**a shows SEM images of the coaxial MWCNT/amor-$Ni(OH)_2$ hybrid. MWCNTs are uniformly covered with $Ni(OH)_2$, and the surface becomes much rougher compared to that of the acid-treated MWCNTs. Their diameters increase to about 15–20 nm, suggesting that a thin layer of $Ni(OH)_2$ was deposited. Figure 2b shows SEM images of the ternary hybrid. Although the diameter of the hybrid is observed to have no significant change before and after PEDOT:PSS wrapping, which suggests the formation of a thin layer of polymer coating, the individual hybrid ropes are found to stick more compactly together with the polymer coating. The transmission electron microscope (TEM) images in Figure 2c,d confirm that the thickness of $Ni(OH)_2$ on the MWCNTs is below 5 nm. The selected-area electron diffraction (SAED) patterns shown on Figure 2c,d only exhibit the diffraction rings from graphitic layers in the MWCNTs at their (002) and (100) planes. The broad and misty halo shown in the SAED patterns confirms that the deposited $Ni(OH)_2$ is amorphous.

Next, X-ray diffraction (XRD) patterns of the MWCNT, MWCNT/Cu_2O, MWCNT/amor-$Ni(OH)_2$, and MWCNT/amor-$Ni(OH)_2$/PEDOT:PSS are shown in **Figure 3**a. MWCNTs display an intensive (002) peak at 25.40° and a minor (100) peak at 42.58°, originating from their graphite-like nature.[31] After depositing Cu_2O, these two peaks become much weaker, while the characteristic peaks of the Cu_2O crystal at the (110), (111), (200), and (311) planes appear at 29.34°, 36.19°, 42.05°, and 61.11°, respectively.[32] Similarly, the MWCNT/amor-$Ni(OH)_2$ and MWCNT/amor-$Ni(OH)_2$/PEDOT:PSS exhibit the weak (002) peaks from the MWCNTs, indicating that the surface of the MWCNTs are mostly covered by $Ni(OH)_2$. The absence of any crystalline $Ni(OH)_2$ characteristic peaks confirms the amorphous structure of the deposited $Ni(OH)_2$, which is in good agreement with the SAED results in Figure 2.

Further, X-ray photoelectron spectroscopy (XPS) was used to characterize the chemical characteristics of the MWCNT/amor-$Ni(OH)_2$ and MWCNT/amor-$Ni(OH)_2$/PEDOT:PSS. Figure 3c shows that the surface of MWCNT/amor-$Ni(OH)_2$ mainly contains Ni, O, C, and a small amount of Cu from the residues of the unetched Cu_2O. The C 1s spectrum (Figure S2a, Supporting Information) has peaks at 284.6 and 285.3 eV from the sp^2 and

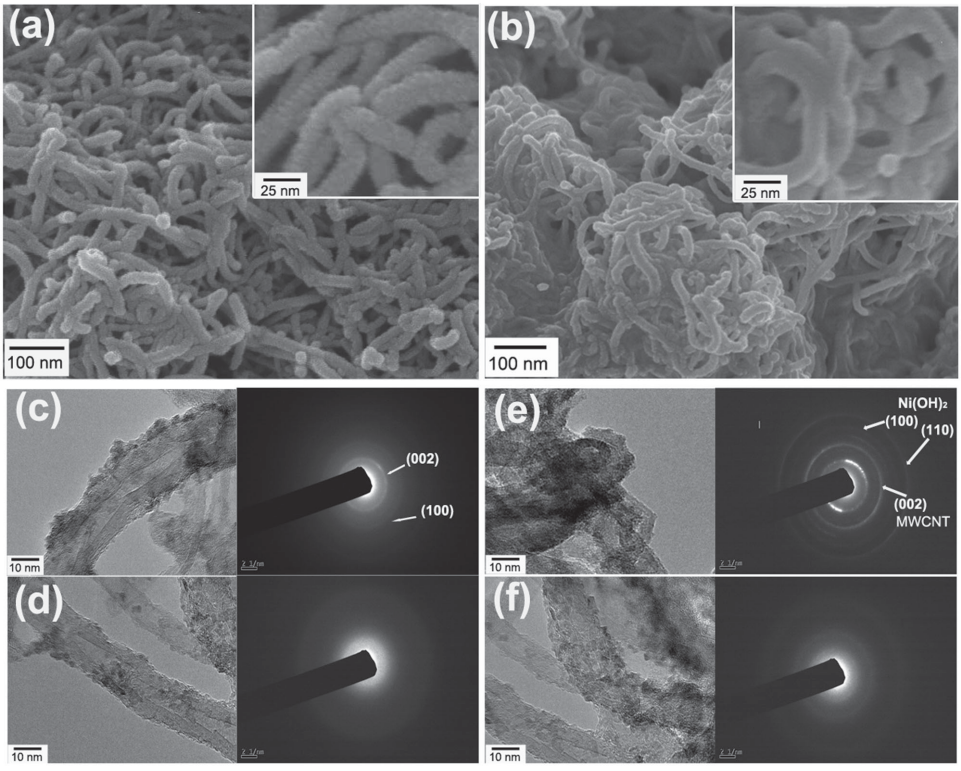

Figure 2. SEM images of a) MWCNT/amor-$Ni(OH)_2$ and b) MWCNT/amor-$Ni(OH)_2$/ PEDOT:PSS. TEM images and the corresponding SAED patterns of c) MWCNT/amor-$Ni(OH)_2$, d) MWCNT/amor-$Ni(OH)_2$/PEDOT:PSS, e) MWCNT/amor-$Ni(OH)_2$ after 3000 charge and discharge cycles, and f) MWCNT/amor-$Ni(OH)_2$/ PEDOT:PSS after 3000 cycles.

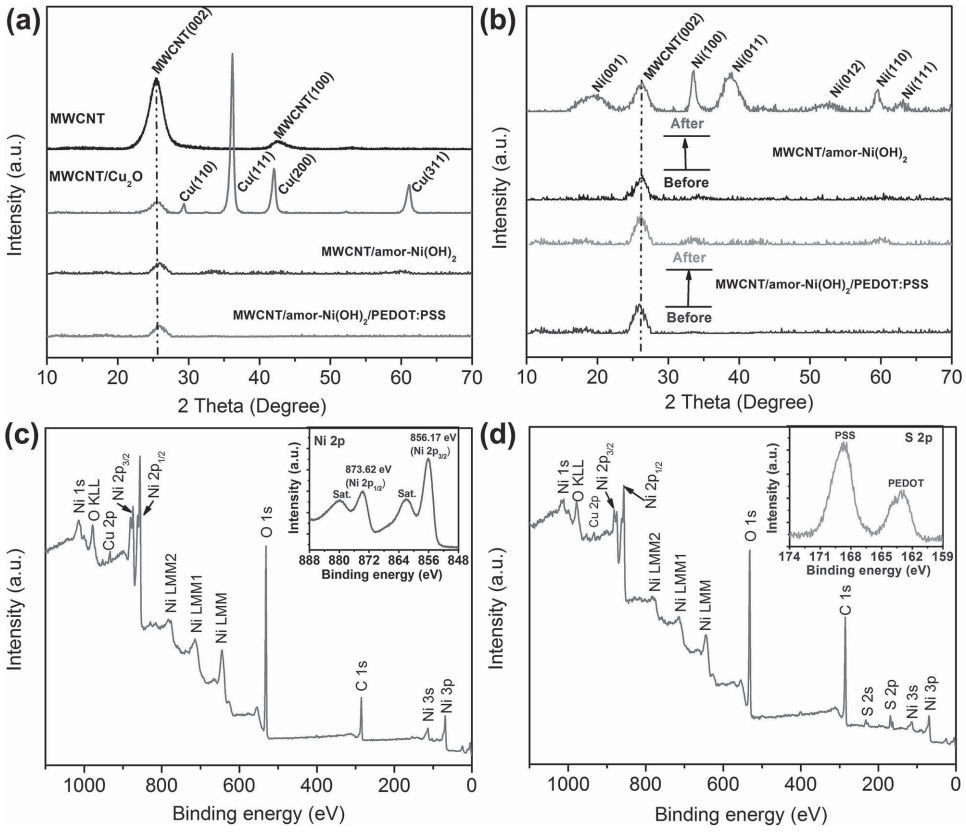

Figure 3. a) XRD patterns of MWCNT, MWCNT/Cu_2O, MWCNT/amor-$Ni(OH)_2$, and MWCNT/amor-$Ni(OH)_2$/PEDOT:PSS, b) Comparison between XRD patterns of MWCNT/amor-$Ni(OH)_2$ and MWCNT/amor-$Ni(OH)_2$/ PEDOT:PSS before and after 3000 charge and discharge cycles. XPS spectra of c) MWCNT/amor-$Ni(OH)_2$ and the inset shows the Ni 2p spectrum, d) MWCNT/amor-$Ni(OH)_2$/ PEDOT:PSS and the inset shows the S 2p spectrum.

sp^3 hybridized C atoms. The C atoms in C–O, C=O, and COO– structures also give peaks at 286.2, 287.4, and 289.1 eV, respectively.[33] The O 1s spectrum (Figure S2b, Supporting Information) has one main peak at 531.2 eV from O atoms in Ni–O structures and three other peaks at 531.8, 532.5, and 533.7 eV from O atoms in carbonyl, phenol, and carboxyl groups, respectively.[34] The C and O XPS spectra indicate that nitric acid treatment introduces oxygen-containing functional groups on the MWCNTs, which not only improve their surface wettability but also generates anchoring sites for $Ni(OH)_2$ deposition.[35] The inset of Figure 3c displays the enlarged Ni 2p XPS spectrum with two major peaks of Ni $2p_{3/2}$ (856.2 eV) and Ni $2p_{1/2}$ (873.6 eV) and their corresponding satellite peaks. The spin-energy separation between the two Ni 2p peaks is at 17.4 eV, agreeing with previous findings on amor-$Ni(OH)_2$.[13] XPS spectrum of the MWCNT/amor-$Ni(OH)_2$/PEDOT:PSS is shown in Figure 3d. The XPS peaks resulting from Ni, O, and C are similar to those observed on the XPS spectrum of the MWCNT/amor-$Ni(OH)_2$. In addition, S 2s (163.1 eV) and S 2p (168.6 eV) peaks from S atoms in the PEDOT:PSS are observed.[30,36]

Furthermore, the specific surface areas of the hybrids are determined from their N_2 adsorption/desorption isotherms (Figure S3a, Supporting Information). The MWCNT/amor-$Ni(OH)_2$ and MWCNT/amor-$Ni(OH)_2$/PEDOT:PSS have a specific surface area of 161 and 127 $m^2\ g^{-1}$, respectively, which are smaller than that of the pristine MWCNTs (200 $m^2\ g^{-1}$). The mass loadings of amor-$Ni(OH)_2$ on MWCNTs were also determined by thermogravimetric analysis (TGA) (Figure S3b, Supporting Information). There are two major weight lost steps on the TGA profile of the MWCNT/amor-$Ni(OH)_2$, which correspond to amor-$Ni(OH)_2$ and MWCNTs, respectively. The mass loading of amor-$Ni(OH)_2$ on MWCNTs was determined to be 49.5 wt% from TGA. Since the MWCNT/amor-$Ni(OH)_2$/PEDOT:PSS contains 10 wt% PEDOT:PSS, the mass loading of amor-$Ni(OH)_2$ in the ternary composite is about 44.6%. We have explored the option of further increasing the mass loading of amor-$Ni(OH)_2$ by depositing more Cu_2O. However, we have found that either the Cu_2O forms large particles, which cannot be completely etched, or crystalline $Ni(OH)_2$ appears on the MWCNTs after replacement. Thus, the mass loading of amor-$Ni(OH)_2$ at around 50 wt% is the optimal loading found in this study.

2.3. Specific Capacitance and Rate Capacity of the Hybrids

We first evaluated the electrochemical performance of the hybrids by cyclic voltammetry (CV) and galvanostatic charge/discharge measurements using a three-electrode cell in 1 M aqueous KOH electrolyte. The MWCNT/amor-$Ni(OH)_2$ was fabricated into electrodes using PVDF as a binder (with the mass ratio of 9:1), while the MWCNT/amor-$Ni(OH)_2$/

PEDOT:PSS was directly used as working electrodes because the PEDOT:PSS coating can hold the materials together without the need of additional polymer binders. In addition, MWCNTs mixed with PVDF binder (with the mass ratio of 9:1) and MWCNTs wrapped with PEDOT:PSS (with the mass ratio of 9:1) without $Ni(OH)_2$ (denoted as MWCNT/PEDOT:PSS) were also measured as reference samples. **Figure 4**a,b show the respective CV curves of MWCNT/amor-$Ni(OH)_2$ and MWCNT/amor-$Ni(OH)_2$/PEDOT:PSS with the potential window from 0 to 0.5 V (vs saturated calomel electrode) at different scan rates. There are two intense redox peaks attributed to the reversible Faradaic reaction between Ni(II) and Ni(III)

$$Ni(OH)_2 + OH^- \leftrightarrow NiOOH + H_2O + e^- \quad (3)$$

The specific gravimetric capacitance (C_s, F g^{-1}) of electrode materials can be calculated using the voltammetric charge integrated from their CV curves according to the equation

$$C_s = \frac{1}{2Vvm}\int_{V_-}^{V_+} i(V)\,dV \quad (4)$$

where the positive and negative sweeps of current $i(V)$ are integrated to obtain the total voltammetric charge. v is the scan rate, and V ($V = V_+ - V_-$) represents the scanned potential window. V used in this study is 0.5 V. m is the mass of the electrode materials. Figure 4d shows that C_s of the MWCNT/amor-$Ni(OH)_2$ and MWCNT/amor-$Ni(OH)_2$/PEDOT:PSS is 1540 and 1454 F g^{-1} at the scan rate of 5 mV s^{-1}, respectively. These are based on the total mass of all active materials in the measured electrodes including MWCNTs, amor-$Ni(OH)_2$, and PEDOT:PSS. CV curves of the two reference samples, MWCNTs and MWCNT/PEDOT:PSS, under a scan rate of 5 mV s^{-1}, are shown in Figure 4c. The MWCNTs display a rectangular shape, which is typical for EDLC. MWCNT/PEDOT:PSS also shows a rectangular-like shape but with a bulge around 0.22 V which is related to the redox reaction of PEDOT.[37] C_s of the two reference samples determined from their CV curves are 58 and 80 F g^{-1}, respectively, which is similar to previously reported results.[37,38] Comparing the C_s of the two references samples to those of the two amor-$Ni(OH)_2$ hybrids, we can conclude that the contribution from EDLC by MWCNTs and PEDOT:PSS to the total capacitance of the hybrids is much smaller (less than 3.8% and 5.2%) than the pseudocapacitance from the amor-$Ni(OH)_2$. In order to better compare the performance of amor-$Ni(OH)_2$ found in this study with the existing literature data reported for $Ni(OH)_2$-based materials, we have further calculated the specific gravimetric capacitance (C'_s) of the hybrids based on the mass of amor-$Ni(OH)_2$ only. It should be noted that amor-$Ni(OH)_2$ counts for 49.5 wt% of the MWCNT/amor-$Ni(OH)_2$ and 44.6 wt% of the MWCNT/amor-$Ni(OH)_2$/PEDOT:PSS. C'_s is 3111 and 3262 F g^{-1} for MWCNT/amor-$Ni(OH)_2$ and MWCNT/amor-$Ni(OH)_2$/PEDOT:PSS, respectively, as shown in Figure 4d. To our knowledge, this is one of the highest gravimetric specific capacitances among all reported $Ni(OH)_2$ materials measured using a three-electrode cell[13–15,17,20,21,27,39–42] (see Table S1, Supporting Information, for detailed comparison), suggesting that efficient surface redox reactions can take place on the thin

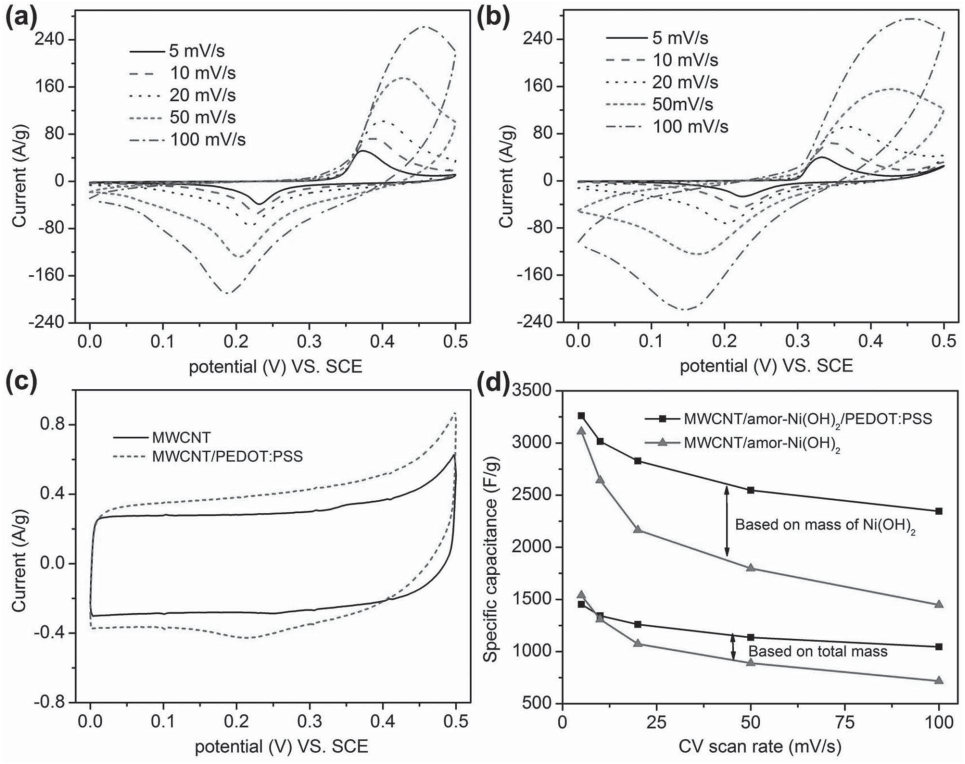

Figure 4. CV curves of a) MWCNT/amor-$Ni(OH)_2$ and b) MWCNT/amor-$Ni(OH)_2$/ PEDOT:PSS at different scan rates in aqueous 1.0 M KOH electrolyte. c) CV curves of MWCNT and MWCNT/PEDOT:PSS at the scan rate of 5 mV s^{-1} in aqueous 1.0 M KOH electrolyte. d) The specific capacitance as function of scan rate of MWCNT/amor-$Ni(OH)_2$ and MWCNT/amor-$Ni(OH)_2$/PEDOT:PSS.

layer of disordered amor-Ni(OH)$_2$ deposited on the MWCNTs. It is worth mentioning that our result is more than two times higher than that of the previously reported pure amor-Ni(OH)$_2$ (1677 F g^{-1}) at the same scan rate of 5 mV s^{-1}.[13] The large specific gravimetric capacitance in this study can be attributed to the synergistic effects in the ternary hybrid architecture as discussed above.

Figure 4d further displays the rate capability of the two hybrids. C'_s of the MWCNT/amor-Ni(OH)$_2$ decreases from 3111 to 1648 F g^{-1} with 53% capacitance retention, when the CV voltage scan rate increases from 5 to 100 mV s^{-1}. In comparison, the MWCNT/amor-Ni(OH)$_2$/PEDOT:PSS exhibits significant improvement, 71.9% of its capacitance being retained. Its rate capability outperforms many previously reported Ni(OH)$_2$ materials[13–15,21,22,25,27,34,39,40,42,43] (see Table S1, Supporting Information, for detailed comparison). The rate capability of pseudocapacitive materials is usually limited by their charge transfer rate and ion diffusion resistance. In our uniquely designed hybrids, the abundance defects within the amor-Ni(OH)$_2$ can improve ion diffusion, which facilitates the efficient transformation between Ni(OH)$_2$ and NiOOH.[44] The MWCNTs serve as conductive highways for electrons. The thin Ni(OH)$_2$ layer prompts the fast and efficient electron transportation between Ni(OH)$_2$ and MWCNTs. Moreover, the conductive PEDOT:PSS can further reduce the electron transfer resistance among MWCNT/amor-Ni(OH)$_2$ ropes, as reflected by the higher capacitance retention observed in the MWCNT/amor-Ni(OH)$_2$/PEDOT:PSS.

The specific gravimetric capacitance of electrode materials can also be calculated from their galvanostatic charge/discharge curves at different current densities using

$$C_s = \frac{i}{\mathrm{d}V/\mathrm{d}t} \quad (5)$$

where i is the discharging current and $\mathrm{d}V/\mathrm{d}t$ is the slope of the discharge curves. The galvanostatic charge/discharge curves of MWCNT/amor-Ni(OH)$_2$ and MWCNT/amor-Ni(OH)$_2$/PEDOT:PSS at the current density from 3 to 20 A g^{-1} are shown in Figure S4, Supporting Information. The calculated C_s and the observed rate capability from the charge/discharge curves are similar to those obtained from their CV curves as shown in Figure 4d. The detailed comparison with the previously reported data obtained using charge/discharge curves is listed in Table S1, Supporting Information. In addition, Figure S5, Supporting Information, also shows that the MWCNT/amor-Ni(OH)$_2$/PEDOT:PSS has high Coulombic efficiencies (near 100%) at the charge/discharge current density up to 20 A g^{-1}, indicating that a large fraction of the redox reactions take place on the surface or near-surface region of amor-Ni(OH)$_2$ in the two hybrids.

2.4. Improved Cycle Life of the Ternary Hybrid

As discussed above, nanoscale structure degradation and Ni ion dissolution are the two key issues compromising the cycle life of many previously reported Ni(OH)$_2$ nanomaterials. The cycle lives of the two hybrids were evaluated by galvanostatic charge/discharge tests at 10 A g^{-1} in a range of 0–0.5 V in 1 M KOH aqueous electrolyte. **Figure 5**a shows that C_s of the MWCNT/amor-Ni(OH)$_2$ drops rapidly from 1103 to 987 F g^{-1} after 200 cycles, and then gradually to 756 F g^{-1} thereafter at 3000 cycles. The instability of the MWCNT/amor-Ni(OH)$_2$ is also substantiated by the change in its electrochemical impedance spectroscopic (EIS) measurements. Figure 5b shows that the composite has much larger equivalent series resistance (from the x-intercept of the Nyquist plot) and higher charge transfer and ion diffusion resistance (from radius of the semicircles and the Warburg region on the Nyquist plot). These electrochemical performance changes are correlated to the structural changes of Ni(OH)$_2$. XRD patterns in Figure 3b indicate that the amor-Ni(OH)$_2$ is gradually transformed to β-crystalline Ni(OH)$_2$ with the appearance of its characteristic peaks at 19.31° (i.e., diffraction of Ni(001)) and 38.34° (i.e., diffraction of Ni(011)). We have also observed the formation of Ni(OH)$_2$ crystals on the TEM image shown in Figure 2e. The SAED pattern

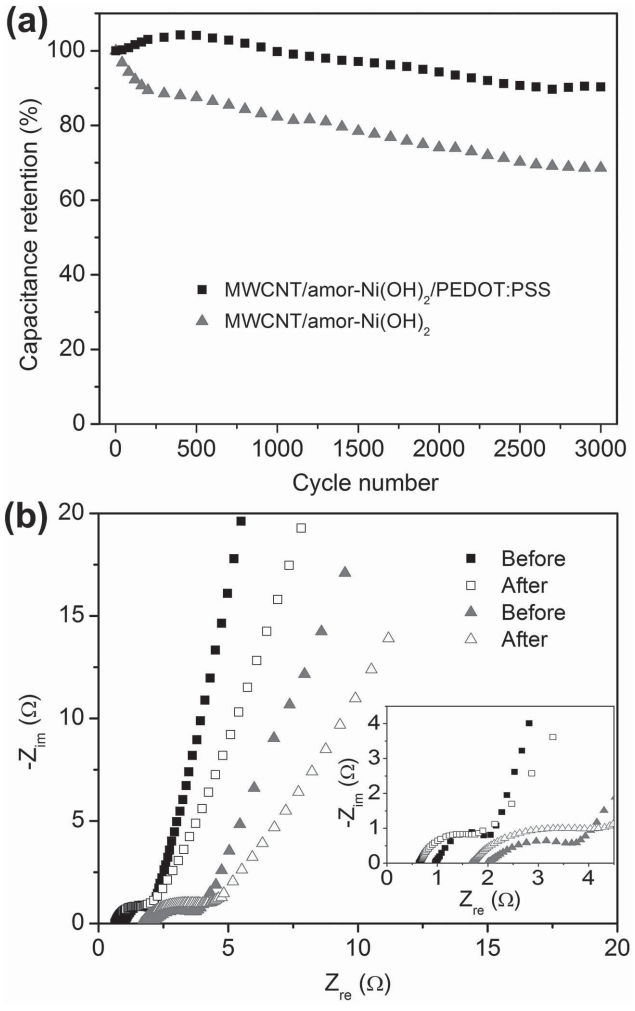

Figure 5. a) Cycle life of MWCNT/amor-Ni(OH)$_2$ and MWCNT/amor-Ni(OH)$_2$/ PEDOT:PSS measured at 10 A g^{-1} in a three-electrode cell with 1 M aqueous KOH electrolyte. b) EIS Nyquist plots of MWCNT/amor-Ni(OH)$_2$ and MWCNT/amor-Ni(OH)$_2$/ PEDOT:PSS before (solid spots) and after (open spots) the 3000 charge and discharge cycles as shown in a). The inset shows the enlarged portion at the high frequency region.

exhibits the diffraction rings from Ni(001) and Ni(011). These structural changes are not surprising as previous studies have reported that α-Ni(OH)$_2$ is not stable in alkaline solution and can be transformed to β-crystalline Ni(OH)$_2$.[44,45] Upon multiple charge/discharge cycles, the ion diffusion inside the amor-Ni(OH)$_2$ supported on MWCNTs may facilitate the formation of the thermodynamically more stable β-Ni(OH)$_2$.

An important design consideration in our ternary hybrid is the wrapping of MWCNT/amor-Ni(OH)$_2$ with PEDOT:PSS so that the cycle life of the MWCNT/amor-Ni(OH)$_2$ can be extended while keeping their excellent specific capacitance and rate capability. Figure 5a shows that the ternary hybrid retains 92% of its original capacitance after 3000 cycles. This performance is not only much better than that of the MWCNT/amor-Ni(OH)$_2$, but also superior to many previously reported Ni(OH)$_2$ materials (see Table S1, Supporting Information, for details).[13,14,17,21,42,46] The improved cycle life of the ternary hybrid can be corroborated with the minimum changes in its equivalent series resistance and ion diffusion resistance (see Figure 5b). XRD (Figure 3b) and TEM (Figure 2f) results also confirm that amor-Ni(OH)$_2$ in the ternary hybrid has minor structural changes after 3000 charge/discharge cycles.

We further extended the cycling test of the MWCNT/amor-Ni(OH)$_2$/PEDOR:PSS to 30 000 cycles at the current density of 20 A g^{-1} in the three-electrode cell in order to demonstrate its long-term stability under high current density (Figure S6, Supporting Information). The electrode retains about 85% of its original capacitance after 20 000 cycles, and still has 77% of its original capacitance after 30 000 cycles. As shown in the insets of Figure S6, Supporting Information, the charge–discharge profiles at different cycling stages (three cycles from each stage) show minor changes in their shapes except for the slightly decreased charge–discharge time. This further confirms the excellent stability of the ternary hybrid.

2.5. Performances of Asymmetric Supercapacitors

To evaluate the practical supercapacitor applications of the ternary hybrid, we have fabricated asymmetric supercapacitors using the MWCNT/amor-Ni(OH)$_2$/PEDOT:PSS as positive electrodes and the rGO/CNT hybrid as negative electrodes. The active electrode materials were coated on two pieces of carbon cloth (1 cm × 1 cm), and then sandwiched with a membrane separator in 1 M aqueous KOH electrolyte. The cell voltage was set as the sum of the potential windows of the positive (0–0.5 V) and negative (–1.0 to 0 V) electrodes at 1.5 V.[25]

The rGO/CNT hybrid was used in this study because of it has better electrochemical performances compared to commonly used activated carbon electrodes.[17,47] The carbon hybrid with a mass ratio of 3:1 between rGO and CNTs was obtained following the previously reported hydrothermal synthesis method.[48,49] The rGO/CNT hybrid is porous (see the SEM image on Figure S7a, Supporting Information) with a specific surface area of 364 m^2 g^{-1} measured by N_2 physisorption (Figure S7b, Supporting Information). The rGO/CNT hybrid was pressed into film electrodes to assemble asymmetric supercapacitors. The CV curves of the rGO/CNT electrode measured using a three-electrode cell 1 M aqueous KOH electrolyte with the scanning voltage from –1 to 0 V are shown in Figure S7c, Supporting Information. The rectangle-like CV curves indicate its EDLC behavior. No obvious IR drops are observed on its galvanostatic charge/discharge curves (Figure S7d, Supporting Information), indicating that it has low internal resistances. The rGO/CNT hybrid has a specific capacitance of 203 F g^{-1} at the current density 1 A g^{-1}, and retains 75% of this specific capacitance when the discharge current was increased to 20 A g^{-1}.

The charge stored by each electrode in an asymmetric supercapacitor depends on the specific capacitance (C_s) of electrode material, the potential window (ΔV) and the mass of electrode materials (m). To balance the charge stored in the two electrodes, the mass ratio of electrode materials is adjusted according to

$$\frac{m^+}{m^-} = \frac{C_s^- \times \Delta V^-}{C_s^+ \times \Delta V^+} \tag{6}$$

In an assembled supercapacitor, the mass loading of the MWCNT/amor-Ni(OH)$_2$/PEDOT:PSS hybrid is about 3.5 mg cm^{-2} and that of the rGO/CNT hybrid is about 12 mg cm^{-2}. The total active materials in each assembled supercapacitor of 1 cm × 1 cm in size are about 15.5 mg.

Figure 6a shows the CV curves of the assembled two-electrode asymmetric supercapacitor with a voltage scan rate from 5 to 150 mV s^{-1}. The CV curves show two redox peaks, which are much broader than those in Figure 4b. Its galvanostatic charge/discharge curves at the current density from 1 to 20 A g^{-1} are shown in Figure 6b. The specific capacitance of the supercapacitor can be determined using

$$C_{\text{cell,m}} = \frac{C_{\text{cell}}}{m^+ + m^-} \tag{7}$$

where C_{cell} are obtained using either the CV curves or galvanostatic discharge curves based on equations similar to Equations (4) and (5), but measured on the two-electrode supercapacitor instead. As shown in Figure 6c,d, the asymmetric supercapacitor demonstrates excellent rate capability and the $C_{\text{cell,m}}$ decreases from 179.8 to 109.6 F g^{-1} when the galvanostatic discharge current increases from 1 to 20 A g^{-1}, or from 159.4 to 102.3 F g^{-1} when the voltage scan rate increases from 5 to 150 mV s^{-1}.

The gravimetric specific energy ($E_{\text{cell,m}}$) and power ($P_{\text{cell,m}}$) density of the supercapacitor are obtained from the equations

$$E_{\text{cell,m}} = C_{\text{cell,m}} \Delta V^2 / (2 \times 3.6) \tag{8}$$

$$P_{\text{cell,m}} = E_{\text{cell,m}} \times 3600 / t_{\text{discharge}} \tag{9}$$

where $t_{\text{discharge}}$ is the discharge time.[25,48]

As shown in the ragone plot on **Figure 7**a, the specific energy density of the supercapacitor reaches 58.5 W h kg^{-1} at the power density of 780 W kg^{-1}, and retains at 30.8 W h kg^{-1} with the high power density of 11.5 kW kg^{-1}. To our knowledge, the asymmetric supercapacitor based on the MWCNT/amor-Ni(OH)$_2$/PEDOT:PSS has one of the highest specific energy and power densities among all reported Ni(OH)$_2$-based supercapacitors

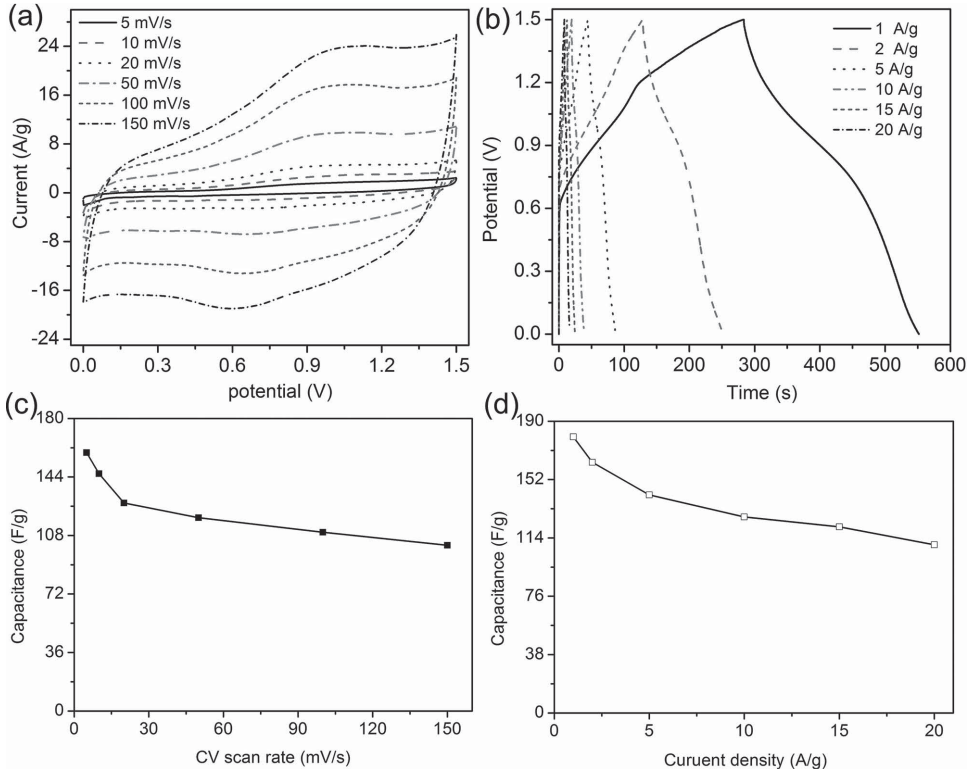

Figure 6. a) CV curves of the assembled MWCNT/amor-Ni(OH)$_2$/PEDOT:PSS//rGO/CNT asymmetric supercapacitor at different scan rates in 1 M aqueous KOH electrolyte with a 1.5 V voltage window. b) Galvanostatic charge/discharge curves of the assembled asymmetric supercapacitor at different current densities. c) The specific capacitance of the supercapacitor measured from CV curves at different scan rates. d) The specific capacitance of the supercapacitor measured from charge/discharge curves at different current densities.

using similar calculation methods.[13,17,50] The detailed comparison between our results with the previously reported data is listed in Table S2, Supporting Information.[13,14,17,19,39,51]

To demonstrate that the supercapacitors can be used as efficient power sources for practical applications, two 1 cm × 1 cm supercapacitors were connected in series to light up two light-emitting diode (LED) indicators (green: 3.0–3.2 V, 20 mA and red: 2.0–2.2 V, 20 mA) for about 9 min after being charged to 3 V in 8 s at the current density of 20 A g^{-1} (see Figure 7b). Moreover, the two supercapacitors in series were also used to drive a motor (Mabuchi RF-500TB, 330 mW) (see Figure 7c and watch the movie in the Supporting Information).

More importantly, the key advantage of the asymmetric supercapacitor is its long cycle life resulting from the uniquely designed ternary hybrid structure in the MWCNT/amor-Ni(OH)$_2$/PEDOT:PSS. **Figure 8** shows that the supercapacitor can retain 90% of its original capacitance after 5000 charge/discharge cycles at 10 A g^{-1} and still maintain at 86% after 30 000 cycles. The initial ten cycles and last ten cycles of the voltage profiles in the inset of Figure 8 show minor changes. The stability performance of the assembled asymmetric supercapacitor is similar to that of its positive electrode, MWCNT/amor-Ni(OH)$_2$/PEDOT:PSS, measured in the three-electrode cell test, which suggests that the cycling performance of the asymmetric supercapacitor is mainly controlled by its positive electrode. The performance of the asymmetric supercapacitor at the first few thousand cycles is evolving. The initial slight increase may be attributed to the improvement of electrode surface wettability and electrolyte ion accessibility.[52] And the following decline may be caused by irreversible surface dissolution of unstable active materials and solid electrolyte interface (SEI) reactions, which have been observed in some previous studies.[25,34,51,53] In our ternary hybrid, the conducting polymer coating helps to stabilize the electrodes by reducing the dissolution of active materials and SEI reactions. Thus, the observed declining trend was extended to about 3000 cycles, in contrast to the fast declay within 1000–2000 cycles observed in many previous reports.[25,34,51,53] After the unstable Ni(OH)$_2$ on the surface is dissoloved and the formation of stable SEI, the performance of the asymmetric supercapacitor became more stable. This cycle life outperforms most of the previously reported Ni(OH)$_2$-based supercapacitors (see Table S2, Supporting Information).[13,14,17,19,25,39,51] The asymmetric supercapacitor tested in two-electrode cell has better cycling performance compared to the electrode tested in three-electrode cell. This may be due to two reasons. First, the three-electrode cell test uses a much larger volume of aqueous electrolyte solution compared to that used in the two-electrode asymmetric supercapacitor. When the electrode materials are immerged in a large volume of electrolyte in the three-electrode cell, the irreversible dissolution of the active materials into electrolyte is more likely to happen because of the fast mass transfer. Second, the three-electrode cell test is an open system where the electrode materials are exposed to the oxygen dissolved in electrolyte from air. In contrast, the

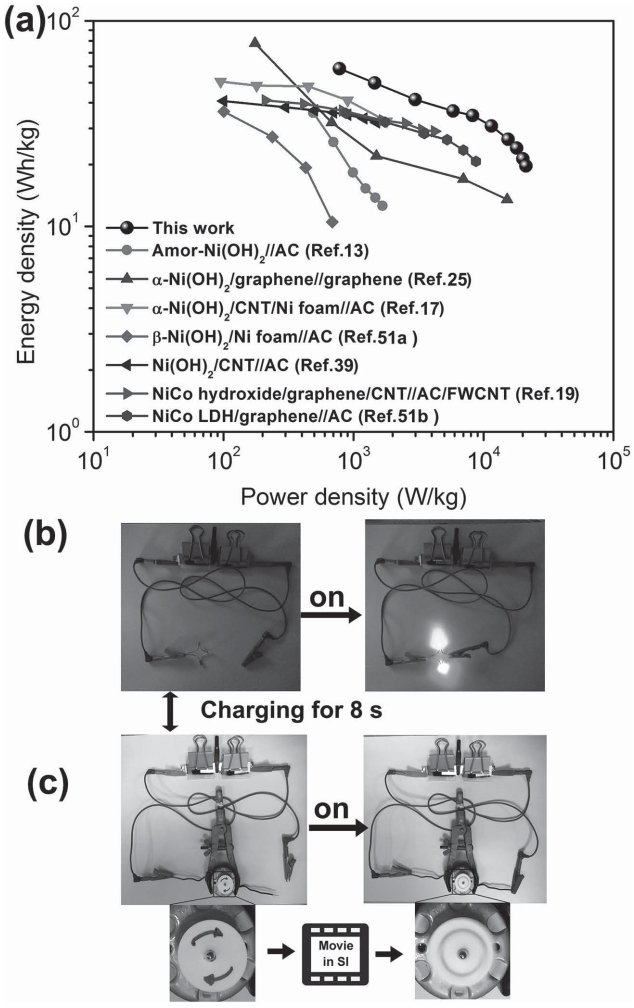

Figure 7. a) Ragone plot of the assembled MWCNT/amor-$Ni(OH)_2$/PEDOT:PSS//rGO/CNT asymmetric supercapacitor in comparison with $Ni(OH)_2$-based symmetric supercapacitors reported in the literature. Photographs showing two asymmetric supercapacitors in series to b) light up two LED indicators in red and green simultaneously, and c) drive a motor (video is shown in the Supporting Information) after charging for 8 s at 20 A g^{-1}.

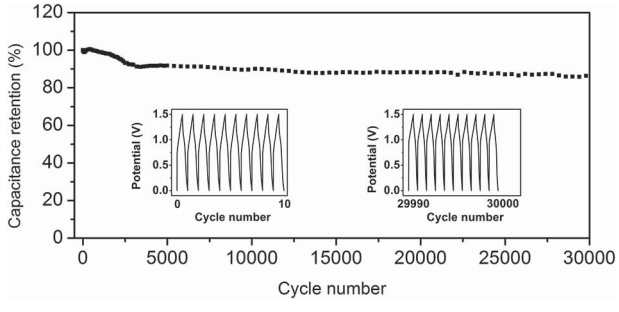

Figure 8. Cycle life of the assembled asymmetric supercapacitor upon 30 000 charge and discharge cycles in 1 M aqueous KOH electrolyte at 10 A g^{-1} galvanostatic charge–discharge current with a potential range of 0–1.5 V. The insets show the first and last ten cycles of charge/discharge profiles of during the test.

partially sealed two-electrode asymmetric supercapacitor significantly limits the oxygen exposure of electrodes.

3. Conclusion

We have successfully synthesized the coaxial ternary hybrid material with a thin layer (<5 nm) of amorphous $Ni(OH)_2$ deposited on nitric acid-treated MWCNTs as the core and a thin conductive polymer (PEDOT:PSS) layer wrapping the core. The amorphous $Ni(OH)_2$ was deposited by a novel "coordinating etching and precipitating" method, which enables large fraction of redox reactions to take place on the surface or near-surface region, resulting in high pseudocapacitance and excellent rate capability. The ternary hybrid has a gravimetric specific capacitance of 3262 F g^{-1} at 5 mV s^{-1} in 1 M aqueous KOH electrolyte and retains 71.9% of its capacitance at 100 mV s^{-1}. More importantly, the PEDOT:PSS layer prevents the degradation of the nanoscale structure of amorphous $Ni(OH)_2$ and Ni ion dissolution upon repeated charges/discharges, resulting in a long cycle life (92% capacitance retention over 3000 cycles and 77% retention over 30 000 cycles under the high current of 20 A g^{-1}). This makes our ternary hybrid superior to most of the previously reported $Ni(OH)_2$ materials. The assembled asymmetric supercapacitor using the ternary hybrid as the positive electrode and the rGO/CNT hybrid as the negative electrode exhibits a gravimetric specific energy density of 58.5 W h kg^{-1} at a power density of 780 W kg^{-1}, and retains at 30.8 W h kg^{-1} with a high power density of 11.5 kW kg^{-1}. The supercapacitor holds 86% of its original capacitance after 30 000 cycles and outperforms most of the previously reported $Ni(OH)_2$ based supercapacitors. Further, two supercapacitors, connected in series, are capable of lighting up two LED indicators simultaneously and driving a motor, demonstrating the excellent practical application potentials. The synthesis method of amorphous $Ni(OH)_2$ and the unique ternary hybrid design that we have demonstrated can be regarded as a general approach to obtain high performance pseudocapacitive materials for supercapacitors with high energy density, rate capability, and long cycle life.

4. Experimental Section

Synthesis of MWCNT/amor-Ni(OH)$_2$: MWCNTs (diameter of 10 nm, FloTube 9000, CNano Technology) were first refluxed in 37% HCl to remove metal catalyst residues, and then in 65% HNO_3 for 4 h to introduce oxygen-containing functional groups. The MWCNT/amor-$Ni(OH)_2$ was synthesized in two steps. In the first step, the coprecipitation process was used to obtain MWCNT/Cu_2O. $CuCl_2$ (1 mL, 0.8 M) solution was slowly dropped into MWCNT (30 mg in 400 mL) aqueous dispersion containing 1×10^{-3} M trisodium citrate in 10 min. Next, NaOH (32 mL, 0.1 M) solution was added dropwise. After stirring for another 10 min, ascorbic acid (15 mL, 0.1 M) was added dropwise, and kept stirring for 30 min before the mixture was aged for 5 h statically. The black mixture gradually turned into dark green color. The resulting MWCNT/Cu_2O was collected by filtration, and then washed by deionized water and ethanol. In the second step, the in situ etching–precipitation process was used to convert Cu_2O into amor-$Ni(OH)_2$. The collected MWCNT/Cu_2O and $Ni(NO_3)_2{\cdot}6H_2O$ (120 mg) were dispersed in ethanol/H_2O (volume ratio = 1:1, 100 mL) by sonication for 30 min. Afterward, $Na_2S_2O_3$ (30 mL, 0.05 M) aqueous solution was slowly added into the dispersion dropwise under continuous stirring, followed by

ageing for another 2 h under stirring. Last, the MWCNT/amor-$Ni(OH)_2$ powders were obtained by filtration, washing with deionized water, and dried at 60 °C for 12 h. For electrochemical characterization of MWCNT/amor-$Ni(OH)_2$ in the three-electrode cell, MWCNT/amor-$Ni(OH)_2$ (about 3.5 mg) and PVDF (as binders) were first mixed at a mass ratio of 9:1 in *N*-methyl pyrrolidone (NMP) by sonication. Then, the mixed electrode material slurry was coated on a 1 × 1 cm area at one end of a carbon cloth (total 1 × 3 cm in rectangle shape), followed by drying at 100 °C in a vacuum oven. The carbon cloth coated with MWCNT/amor-$Ni(OH)_2$ was used as the working electrode.

Synthesis of MWCNT/amor-Ni(OH)$_2$/PEDOT:PSS: PEDOT:PSS solution (2 mg in 154 mg of water dispersion of 1.3 wt%) was added dropwise into the MWCNT/amor-$Ni(OH)_2$ aqueous dispersion (18 mg, 30 mL) under stirring. The mixture was further stirred for 5 h. Afterward, the resulting solids were collected by filtration. It was noted that the filtrate became colorless, different from the initial blue PEDOT:PSS solution, indicating that PEDOT:PSS was anchored on the hybrid. MWCNT/amor-$Ni(OH)_2$/PEDOT:PSS electrodes were prepared using the similar method as described earlier without adding PVDF binders.

Synthesis of rGO/CNT Hybrid: The hybrid was synthesized using a modified method from our previous publication.[48] Briefly, graphene oxide (GO) was prepared by the modified Hummers' method using natural graphite. CNTs (1.4 nm in diameter, Carbon Solution) were also treated in HCl and HNO_3 similar to the MWCNTs as described above. A homogeneous GO/CNT (at the mass ratio of 3:1) mixture was obtained by sonicating predetermined amount of acid-treated CNTs in GO (10 mL, 2 mg mL^{-1}) aqueous solution. The mixture was then transferred to a Teflon-lined stainless steel autoclave for 18 h hydrothermal treatment at 180 °C. Afterward, the rGO/CNT hybrid was freeze-dried and crushed into powders. The rGO/CNT electrodes were fabricated using PVDF as binder.

Assembly of Asymmetric Supercapacitor: MWCNT/amor-$Ni(OH)_2$/PEDOT:PSS and rGO/CNT were used as positive and negative electrodes, respectively, at the mass ratio of 1:3.5. The two film electrodes and a piece of separator membrane (Nippon Kodoshi Co.) were sandwiched together to form the complete device.

Material Characterization: The morphology of the materials was examined by SEM (JEOL, JSM6701, 5 kV) and TEM (JEM-2010, JEOL, 120.0 kV). The crystallographic structures of the materials were characterized by a powder XRD system (Bruker, AXS D8) and the SAED performed by JEM-2010 TEM. The chemical composition of the material surfaces was analyzed by XPS (PHI, Quantera). The specific surface areas of the materials were measured using a surface area analyzer (QuantaChrome, Autosorb-6B) and calculated by the Brunauer–Emmett–Teller method. Samples were degassed at 120 °C for 10 h under vacuum (<0.01 mbar) before the surface area test. The mass loading of $Ni(OH)_2$ was determined in thermogravimetric analysis (Perkin Elmer, Diamond FTA32 TG/DTA).

Electrochemical Characterization: The electrochemical tests of various materials were performed using a three-electrode cell in 1 M aqueous KOH electrolyte with a platinum wire as the counter electrode, a saturated calomel electrode as the reference electrode, and the working electrode prepared as described early. The performance of the asymmetric supercapacitors was evaluated by measuring the assembled two-electrode cells. CV, galvanostatic charge/discharge, and capacitance retention tests were carried out by the potentiostat (CHI 660D). EIS spectra were taken by the potentiostat (VersaSTAT 4).

Supporting Information

Supporting Information is available from the Wiley Online Library or from the author.

Acknowledgements

This work was supported by Ministry of Education, Singapore (MOE2011-T2-2-062 and 2013-T1-002-132), and Asian Office of Aerospace Research and Development of the U.S. Air Force (FA23861314110).

Received: September 25, 2014
Revised: November 24, 2014
Published online: January 12, 2015

[1] B. E. Conway, *Electrochemical Supercapacitors, Scientific Fundamentals and Technological Applications*, Springer, New York **1999**.
[2] F. Beguin, E. Frackowiak, *Supercapacitors: Materials, Systems and Applications*, Wiley-VCH, Weinheim, Germany **2013**.
[3] P. Simon, Y. Gogotsi, B. Dunn, *Science* **2014**, *343*, 1210.
[4] a) M. Winter, R. J. Brodd, *Chem. Rev.* **2004**, *104*, 4245; b) V. Augustyn, J. Come, M. A. Lowe, J. W. Kim, P. L. Taberna, S. H. Tolbert, H. D. Abruna, P. Simon, B. Dunn, *Nat. Mater.* **2013**, *12*, 518; c) K. Wang, H. Wu, Y. Meng, Z. Wei, *Small* **2014**, *10*, 14; d) P. Chen, H. Chen, J. Qiu, C. Zhou, *Nano Res.* **2010**, *3*, 594.
[5] G. Wang, L. Zhang, J. Zhang, *Chem. Soc. Rev.* **2012**, *41*, 797.
[6] J. Yan, Q. Wang, T. Wei, Z. Fan, *Adv. Energy Mater.* **2014**, *4*, 1300816.
[7] L. Feng, Y. Zhu, H. Ding, C. Ni, *J. Power Sources* **2014**, *267*, 430.
[8] M. C. Bernard, R. Cortes, M. Keddam, H. Takenouti, P. Bernard, S. Senyarich, *J. Power Sources* **1996**, *63*, 247.
[9] S. Deabate, F. Henn, S. Devautour, J. C. Giuntini*J. Electrochem. Soc.* **2003**, *150*, J23.
[10] Y. Hou, Y. Cheng, T. Hobson, J. Liu, *Nano Lett.* **2010**, *10*, 2727.
[11] Q. Lu, J. G. Chen, J. Q. Xiao, *Angew. Chem. Int. Ed.* **2013**, *52*, 1882.
[12] a) U. M. Patil, K. V. Gurav, V. J. Fulari, C. D. Lokhande, O. S. Joo, *J. Power Sources* **2009**, *188*, 338; b) J. Li, W. Zhao, F. Huang, A. Manivannan, N. Wu, *Nanoscale* **2011**, *3*, 5103; c) S. Yang, X. Wu, C. Chen, H. Dong, W. Hu, X. Wang, *Chem. Commun.* **2012**, *48*, 2773.
[13] H. B. Li, M. H. Yu, F. X. Wang, P. Liu, Y. Liang, J. Xiao, C. X. Wang, Y. X. Tong, G. W. Yang, *Nat. Commun.* **2013**, *4*, 1894.
[14] J. Ji, L. L. Zhang, H. Ji, Y. Li, X. Zhao, X. Bai, X. Fan, F. Zhang, R. S. Ruoff, *ACS Nano* **2013**, *7*, 6237.
[15] H. Wang, H. S. Casalongue, Y. Liang, H. Dai, *J. Am. Chem. Soc.* **2010**, *132*, 7472.
[16] J. Xie, X. Sun, N. Zhang, K. Xu, M. Zhou, Y. Xie, *Nano Energy* **2013**, *2*, 65.
[17] Z. Tang, C.-H. Tang, H. Gong, *Adv. Funct. Mater.* **2012**, *22*, 1272.
[18] D. Ghosh, S. Giri, M. Mandal, C. K. Das, *RSC Adv.* **2014**, *4*, 26094.
[19] Y. Cheng, H. Zhang, C. V. Varanasi, J. Liu, *Energy Environ. Sci.* **2013**, *6*, 3314.
[20] X. Wang, C. Yan, A. Sumboja, J. Yan, P. S. Lee, *Adv. Energy Mater.* **2014**, *4*, 1301240.
[21] N. A. Alhebshi, R. B. Rakhi, H. N. Alshareef, *J. Mater. Chem. A* **2013**, *1*, 14897.
[22] S. Chen, J. Zhu, H. Zhou, X. Wang, *RSC Adv.* **2011**, *1*, 484.
[23] L. Wei, W. Jiang, K. Goh, Y. Chen, *Polym. Eng. Sci.* **2014**, *54*, 336.
[24] J. Nai, Y. Tian, X. Guan, L. Guo, *J. Am. Chem. Soc.* **2013**, *135*, 16082.
[25] J. Yan, Z. Fan, W. Sun, G. Ning, T. Wei, Q. Zhang, R. Zhang, L. Zhi, F. Wei, *Adv. Funct. Mater.* **2012**, *22*, 2632.
[26] Y. Wang, S. Gai, N. Niu, F. He, P. Yang, *J. Mater. Chem. A* **2013**, *1*, 9083.
[27] S. Chen, J. Duan, Y. Tang, S. Zhang Qiao, *Chem. Eur. J.* **2013**, *19*, 7118.
[28] C. Liu, Y. Li, *J. Alloys Comp.* **2009**, *478*, 415.
[29] a) G. H. Yu, L. B. Hu, N. A. Liu, H. L. Wang, M. Vosgueritchian, Y. Yang, Y. Cui, Z. A. Bao, *Nano Lett.* **2011**, *11*, 4438; b) G. A. Snook, P. Kao, A. S. Best, *J. Power Sources* **2011**, *196*, 1.
[30] Z. Su, C. Yang, C. Xu, H. Wu, Z. Zhang, T. Liu, C. Zhang, Q. Yang, B. Li, F. Kang, *J. Mater. Chem. A* **2013**, *1*, 12432.
[31] Y. K. Kim, H. Park, *Energy Environ. Sci.* **2011**, *4*, 685.

[32] J. C. Park, J. Kim, H. Kwon, H. Song, *Adv. Mater.* **2009**, *21*, 803.
[33] J. Shen, A. Liu, Y. Tu, H. Wang, R. Jiang, J. Ouyang, Y. Chen, *Electrochim. Acta* **2012**, *78*, 122.
[34] Z. Wu, X.-L. Huang, Z.-L. Wang, J.-J. Xu, H.-G. Wang, X.-B. Zhang, *Sci. Rep.* **2014**, *4*, 3669.
[35] M. Sathiya, A. S. Prakash, K. Ramesha, J. M. Tarascon, A. K. Shukla, *J. Am. Chem. Soc.* **2011**, *133*, 16291.
[36] Y. Xia, K. Sun, J. Ouyang, *Energy Environ. Sci.* **2012**, *5*, 5325.
[37] K. Lota, V. Khomenko, E. Frackowiak, *J. Phys. Chem. Solids* **2004**, *65*, 295.
[38] D. Antiohos, G. Folkes, P. Sherrell, S. Ashraf, G. G. Wallace, P. Aitchison, A. T. Harris, J. Chen, A. I. Minett, *J. Mater. Chem.* **2011**, *21*, 15987.
[39] Y.-G. Wang, L. Yu, Y.-Y. Xia, *J. Electrochem. Soc.* **2006**, *153*, A743.
[40] Y. Fu, J. Song, Y. Zhu, C. Cao, *J. Power Sources* **2014**, *262*, 344.
[41] Y. Yang, L. Li, G. Ruan, H. Fei, C. Xiang, X. Fan, J. M. Tour, *ACS Nano* **2014**, *8*, 9622.
[42] X. Chen, C. Long, C. Lin, T. Wei, J. Yan, L. Jiang, Z. Fan, *Electrochim. Acta* **2014**, *137*, 352.
[43] D. P. Dubal, G. S. Gund, C. D. Lokhande, R. Holze, *ACS Appl. Mater. Interfaces* **2013**, *5*, 2446.
[44] A. Van der Ven, D. Morgan, Y. S. Meng, G. Ceder, *J. Electrochem. Soc.* **2006**, *153*, A210.
[45] a) M. B. J. G. Freitas, *J. Power Sources* **2001**, *93*, 163; b) P. Oliva, J. Leonardi, J. F. Laurent, C. Delmas, J. J. Braconnier, M. Figlarz, F. Fievet, A. D. Guibert, *J. Power Sources* **1982**, *8*, 229.
[46] H. W. Park, Y. T. Ju, S.-M. Park, K. C. Roh, *RSC Adv.* **2014**, *4*, 567.
[47] a) C.-H. Tang, X. Yin, H. Gong, *ACS Appl. Mater. Interfaces* **2013**, *5*, 10574; b) D. Yu, L. Dai, *J. Phys. Chem. Lett.* **2009**, *1*, 467.
[48] D. Yu, K. Goh, H. Wang, L. Wei, W. Jiang, Q. Zhang, L. Dai, Y. Chen, *Nat. Nanotechnol.* **2014**, *9*, 555.
[49] a) M. Beidaghi, C. Wang, *Adv. Funct. Mater.* **2012**, *22*, 4501; b) Q. Cheng, J. Tang, J. Ma, H. Zhang, N. Shinya, L.-C. Qin, *Phys. Chem. Chem. Phys.* **2011**, *13*, 17615.
[50] a) C.-C. Hu, J.-C. Chen, K.-H. Chang, *J. Power Sources* **2013**, *221*, 128; b) H. Wang, Y. Liang, T. Mirfakhrai, Z. Chen, H. Casalongue, H. Dai, *Nano Res.* **2011**, *4*, 729; c) P. Lu, F. Liu, D. Xue, H. Yang, Y. Liu, *Electrochim. Acta* **2012**, *78*, 1.
[51] a) J. Huang, P. Xu, D. Cao, X. Zhou, S. Yang, Y. Li, G. Wang, *J. Power Sources* **2014**, *246*, 371; b) W. Zhang, C. Ma, J. Fang, J. Cheng, X. Zhang, S. Dong, L. Zhang, *RSC Adv.* **2013**, *3*, 2483; c) C. Long, T. Wei, J. Yan, L. Jiang, Z. Fan, *ACS Nano* **2013**, *7*, 11325.
[52] Z. Wu, X.-L. Huang, Z.-L. Wang, J.-J. Xu, H.-G. Wang, X.-B. Zhang, *Sci. Rep.* **2014**, *4*, 3669.
[53] R. S. Borges, A. L. M. Reddy, M.-T. F. Rodrigues, H. Gullapalli, K. Balakrishnan, G. G. Silva, P. M. Ajayan, *Sci. Rep.* **2013**, *3*, 2572.